

## AdS/CFT correspondence in hyperbolic lattices

Jingming Chen<sup>1</sup>, Feiyu Chen<sup>2</sup>, Linyun Yang<sup>1</sup>, Yuting Yang<sup>3</sup>, Zihan Chen<sup>1</sup>, Ying Wu<sup>4</sup>, Yan Meng<sup>1</sup>, Bei Yan<sup>1</sup>, Xiang Xi<sup>1</sup>, Zhenxiao Zhu<sup>1</sup>, Minqi Cheng<sup>1</sup>, Gui-Geng Liu<sup>5</sup>, Perry Ping Shum<sup>1</sup>, Hongsheng Chen<sup>6</sup>, Rong-Gen Cai<sup>7</sup>, Run-Qiu Yang<sup>8,\*</sup>, Yihao Yang<sup>6,†</sup>, Zhen Gao<sup>1,9,10,‡</sup>

<sup>1</sup>Department of Electrical and Electronic Engineering, Southern University of Science and Technology, Shenzhen 518055, China.

<sup>2</sup>Institute of High Energy Physics, Chinese Academy of Sciences, Beijing 100049, China.

<sup>3</sup>School of Materials Science and Physics, China University of Mining and Technology, Xuzhou 221116, China.

<sup>4</sup>School of Physics, Nanjing University of Science and Technology, Nanjing 210094, China.

<sup>5</sup>Division of Physics and Applied Physics, School of Physical and Mathematical Sciences, Nanyang Technological University, 21 Nanyang Link, Singapore 637371, Singapore.

<sup>6</sup>Interdisciplinary Center for Quantum Information, State Key Laboratory of Modern Optical Instrumentation, ZJU-Hangzhou Global Science and Technology Innovation Center, College of Information Science and Electronic Engineering, ZJU-UIUC Institute, Zhejiang University, Hangzhou 310027, China.

<sup>7</sup>CAS Key Laboratory of Theoretical Physics, Institute of Theoretical Physics, Chinese Academy of Sciences, Beijing 100190, China.

<sup>8</sup>Center for Joint Quantum Studies and Department of Physics, School of Science, Tianjin University, Tianjin 300350, China.

<sup>9</sup>State Key Laboratory of Optical Fiber and Cable Manufacture Technology, Southern University of Science and Technology, Shenzhen, Guangdong, China.

<sup>10</sup>Guangdong Key Laboratory of Integrated Optoelectronics Intellisense, Southern University of Science and Technology, Shenzhen, 518055, China.

\*†‡Corresponding author Email: gaoz@sustech.edu.cn (Z.G.); yangyihao@zju.edu.cn (Y.H.Y.); aqiu@tju.edu.cn (R.-Q.Y)

The celebrated anti-de Sitter/conformal field theory (AdS/CFT) correspondence<sup>1-3</sup>, also known as the gravity/gauge duality, posits a dual relationship between the quantum gravity in an AdS spacetime and the CFT defined on its lower-dimensional boundary. This correspondence not only offers profound insights into the enigmatic nature of quantum gravity but also shows mighty power in addressing strongly-correlated systems. However, despite its importance in contemporary physics, the AdS/CFT correspondence remains a conjecture, and further experimental investigation is highly sought after. Here, we present the first experimental exploration of this conjecture by testing its core corollary: the leading-order effects of a strongly-coupled CFT can be exactly described by a weakly-coupled classical field in a higher-dimensional AdS spacetime. Through measuring the bulk entanglement entropy (BEE) and boundary-boundary correlation function (BBCF) of scalar fields in both conventional type-I and previously overlooked type-II hyperbolic lattices, serving as the discretized regularizations of spatial geometries of pure  $\text{AdS}_{2+1}$  spacetime and  $\text{AdS}_{2+1}$  black hole, respectively, we experimentally confirm that BEE exhibits a logarithmic scaling with the subsystem size, following the Ryu-Takayanagi (RT) formula, while BBCF showcases an exponential law dependence on the boundary separation, the scaling dimension of which conforms to the Klebanov-Witten (KW) relation, both of which align remarkably well with the established CFT outcomes. This heuristic experimental effort opens a new avenue for in-depth investigations on the gravity/gauge duality and extensive exploration of quantum-gravity-inspired phenomena in classical systems.

The anti-de Sitter spacetime is a negatively curved spacetime with constant curvature, which leads to fascinating and unique physical properties that diverge from our familiar experience in the flat Minkowski spacetime. It serves as a backdrop for various physical theories and models,

including the celebrated holographic principle<sup>4,5</sup>. This principle asserts that the physical degrees of freedom within bulk may be represented on its lower-dimensional boundary. The anti-de Sitter /conformal field theory (AdS/CFT) correspondence<sup>1-3</sup> constitutes the most successful embodiment of holography, featuring a remarkable duality between a d+1-dimensional weakly-coupled quantum gravity theory in an AdS spacetime and a d-dimensional strongly-coupled CFT on its boundary. This correspondence not only significantly improves our comprehension of quantum gravity, holography, and black holes, but also provides a valuable analytical framework for the study of strongly interacting systems in both nuclear<sup>8</sup> and condensed matter physics<sup>9</sup>.

Over the past decades, numerous interdisciplinary concepts from general relativity, thermodynamics, quantum information, and quantum field theory have been integrated into the AdS/CFT dictionary. The foremost among these concepts are the entanglement entropy and correlation function that respectively quantify the degree of entanglement and correlation among subsystems or operators, holding profound significance for understanding the nature of quantum gravity and the dynamics of quantum fields. Under the AdS/CFT correspondence framework, regarding the CFT side, the most prominent holographic result of the entanglement entropy is the Ryu-Takayanagi (RT) formula<sup>3</sup> (also known as “area law”) which builds a bridge connecting the entanglement entropy of the boundary CFT and the bulk geometry:

$$S(A) = \frac{\text{Area}(\Gamma_A^{min})}{4G_N^{(d+1)}}, \quad (1)$$

where  $S(A)$  is the entanglement entropy for boundary subsystem  $A$ ,  $\Gamma_A^{min}$  is the codimension-two minimal surface in the bulk enclosing  $A$ , and  $G_N^{(d+1)}$  is the d+1-dimensional Newton constant. Besides, the most critical holographic result of the correlation function is the Klebanov-Witten

(KW) relation<sup>2,6</sup>, which associates the conformal dimension  $\Delta$  of scalar operator in the boundary CFT with the mass  $m_S$  of the bulk scalar field following:

$$\Delta(\Delta - d_b) = m_S^2 \ell^2, \quad (2)$$

where  $\ell^2$  is the AdS radius-squared and  $d_b$  represents the boundary dimension. These theoretical advances inspire an established paradigm for exploring entanglement entropy and correlation function in a CFT, which are notoriously difficult to measure in practice due to the intricate many-body interactions, using a dual classical gravity description. On the other hand, in the light of AdS/CFT correspondence, the leading-order effects of entanglement entropy and correlation function in a strongly-coupled CFT can be described by their holographic counterparts of a weakly-coupled field within the classical AdS gravity background. This fundamental corollary motivates a paradigm-shifting experimental approach to explore the AdS/CFT correspondence by measuring the entanglement entropy and correlation function within an AdS spacetime to scrutinize whether these quantities could precisely reveal the known behaviors of a dual conformal field.

Inspired by recent theoretical and experimental breakthroughs in exploring complex field theories<sup>10-16</sup> and novel topological matters and states in hyperbolic lattices<sup>17-23</sup>, here, we report the first experimental investigation of the AdS/CFT correspondence by testing the aforementioned corollary in hyperbolic lattices that serve as discretized regularizations of AdS<sub>2</sub> spaces. Besides the conventional type-I hyperbolic lattice that corresponds to a pure AdS<sub>2</sub> space, we propose a previously overlooked type-II hyperbolic lattice that corresponds to the spatial geometry of an AdS<sub>2+1</sub> black hole. These two types of hyperbolic lattices are experimentally realized in electric circuit networks, which have previously been proposed to explore scalar field dynamics in AdS<sub>2</sub> space<sup>11,16</sup>. Using time-dynamic pulse measurements, we experimentally identify distinct geodesic

behaviors in hyperbolic circuits without and with an analogue black hole. Furthermore, using pump-probe measurements, we experimentally measure the bulk entanglement entropy (BEE) and boundary-boundary correlation function (BBCF) of scalar fields in hyperbolic circuits, and uncover the logarithmic scaling law of BEE with subsystem size, following the RT formula in the  $\text{AdS}_{2+1}/\text{CFT}_{1+1}$  correspondence, and the exponential law dependence of BBCF on boundary separation, the scaling dimension of which conforms to the KW relation in the  $\text{EAdS}_2/\text{CFT}_{0+1}$  (Euclidean  $\text{AdS}_2$ ) correspondence. These observed regularities of entanglement entropy and correlation function precisely coincide with the known results of their holographic counterparts in a CFT. Our work represents a step towards a new paradigm for studying holographic models and negatively curved space dynamics with tabletop experiments in the laboratory.

We start with the fundamental classification for all 2+1-dimensional spacetimes of constant negative curvature based on their topologies. Two noteworthy cases within this classification are the pure  $\text{AdS}_{2+1}$  spacetime (Fig. 1a) and the  $\text{AdS}_{2+1}$  black hole (commonly called Banados–Teitelboim–Zanelli (BTZ) black hole<sup>24</sup>) (Fig. 1b). To be more intuitive, their corresponding spatial sections at a time-constant slice can be represented as a two-sheet hyperboloid (Fig. 1c) and a one-sheet hyperboloid (Fig. 1d), respectively<sup>30</sup> (see Methods). These two geometries can be continuously projected as planar hyperbolic models, i.e., “Poincaré disk” (Fig. 1e) and “Poincaré ring” (Fig. 1f), respectively (see Methods), preserving the local constant negative curvature and global topology. More intriguingly, these two types of planar Poincaré models can be further discretized as type-I hyperbolic lattice<sup>10-23</sup> (Fig. 1g) and type-II hyperbolic lattice (Fig. 1h), respectively, via regular polygons tessellation. Furthermore, based on the rigorous map between the tight-bind model and electric circuit network<sup>11,17-19</sup>, these two types of hyperbolic lattice can be experimentally equivalent to type-I hyperbolic circuit (Fig. 1i) and type-II hyperbolic circuit

(Fig. 1j), respectively. Consequently, given this top-down geometric consistency, the physical properties of continuous scalar fields propagating in the  $\text{AdS}_2$  spaces can be well-preserved by the discretized scalar fields (i.e., voltage field) in the hyperbolic circuits, especially in the long-wavelength regime.

In our experiments, we specifically implement a typical finite type-I (type-II) hyperbolic circuit denoted by the Schläfli symbol  $\{3, 7\}$ , which represents a regular tessellation of Poincaré disk (Poincaré ring) by 7 copies of 3-sided polygons meeting at each vertex (see Extended Data Fig. 2). As shown in Fig. 2a and Fig. 2b, each node is grounded through an inductor  $L$  and coupled with its seven nearest neighbors by seven capacitors  $C$ . Moreover, to implement the Dirichlet boundary conditions<sup>11</sup>, all boundary nodes are grounded by extra capacitors to ensure that each node is capacitively coupled to seven other nearest components.

### **Time-dynamic identification of geodesics**

We begin our experiments with the dynamic demonstration of geodesics in type-I and type-II hyperbolic circuits via time-resolved measurements (see Methods). In the experiment, a temporal voltage pulse (green line in Fig. 2c) is fed into a type-I (type-II) hyperbolic circuit from boundary node31 (node300). The corresponding frequency spectrum of the pulse (green line in Fig. 2d) is broad enough to cover the measured impedance spectrums of type-I (red line in Fig. 2d) and type-II (blue line in Fig. 2d) hyperbolic circuits, ensuring all intrinsic modes are excited to approximate the continuum response<sup>9</sup>. The dynamic evolution of pulse in hyperbolic circuits gives rise to changing instantaneous phases in all nodes, we mark the time at  $1.55\mu\text{s}$  (black line in Fig. 2c) and  $1.55\mu\text{s} + 3.7\mu\text{s}$  (black and grey lines in Fig. 2c) and plot the profile of instantaneous phases of type-I and type-II hyperbolic circuits in Fig. 2e and Fig. 2f (see Methods and Extended Data Fig. 3), respectively, where the phase fronts (black lines in Fig. 2e and Fig. 2f) can be easily

identified by the positions of equal instantaneous phase. Therefore, the trajectories of pulse propagation, i.e., the geodesics, can be directly drawn out according to their orthogonality to the phase fronts, as highlighted by white curves in Fig. 2e and Fig. 2f. It is evident that the geodesics in type-I hyperbolic circuits are arcs whose two ends are perpendicular to the boundary. In contrast, in type-II hyperbolic circuits, the geodesics are bow-shaped curves that wrap around the horizon (white dashed line in Fig. 2f). These experimental results are precisely consistent with the theoretical conclusions in the continuum (see Supplementary Information S2).

Next, we experimentally measure the BEE and BBCF of scalar fields in type-I and type-II hyperbolic circuits, using static pump-probe measurements (see Methods).

### **Measurements of holographic quantities in the type-I hyperbolic circuit**

We first investigate the case in the pure AdS<sub>2</sub> background. We start by considering the BEE in the Poincaré disk which serves as a spatial slice of the AdS<sub>2+1</sub>/CFT<sub>1+1</sub> setup with time fixed. According to the AdS/CFT correspondence, as illustrated in the bottom of Fig. 3a, the entanglement entropy  $S_S(W_A)$  for an entanglement wedge  $W_A$  (yellow region) as a subsystem of bulk weakly-coupled scalar field is equal to the entanglement entropy  $S(A)$  for an interval  $A$  as a subsystem of boundary strongly-coupled CFT. Note that  $S(A)$  is known to exhibit the logarithmic scaling with the  $A$  size as<sup>3,7</sup>:

$$S(A) = \frac{c}{3} \log \left[ \frac{2}{a} \sin \left( \frac{\theta_A}{2} \right) \right], \quad (3)$$

where  $c = 3/2G_N^{(3)}$  is central charge and  $a$  is radial cutoff, meanwhile following the two-dimensional (2D) zero-temperature RT formula:  $S(A) = \frac{c}{6} L_{\gamma_{\mathcal{D}}(A)}$ , where  $L_{\gamma_{\mathcal{D}}(A)}$  is the length of geodesic  $\gamma_{\mathcal{D}}(A)$  (see Supplementary Information S3.1). To test whether  $S_S(W_A)$  aligns with these

CFT conclusions, we experimentally measure  $S_S(W_A)$  utilizing the scalar field in a type-I hyperbolic circuit. This methodology is underpinned by two principal grounds: First, theoretically,  $S_S(W_A)$  is calculated based on the ground state of scalar field, the weakly-coupled nature of which validates the free field theory approximation in the bulk and this ground state can be particularly determined as a direct product of infinite single-quasiparticle states. Each of these states manifests as the fundamental mode of the Laplace-Beltrami operator on the Poincaré disk (top in Fig. 3a). Second, in the long-wavelength limit, this mode in the continuum can be effectively reproduced by the discretized fundamental model of the type-I hyperbolic circuit (top in Fig. 3b) (see Supplementary Information S4.1). For reference, the radial mode profiles of both the continuum and the circuit are compared, as shown in Fig. 3c, presenting a remarkable quantitative agreement. Therefore, with a many-quasiparticle state consideration for the circuit single-quasiparticle state,  $S_S(W_A)$  (equivalently, Von Neumann entropy since the entire bulk system is in a pure state) can be computed via equation (see Methods):

$$S_S(W_A) = \frac{1}{2} \log \left( \frac{p_k(p_k - 1)}{\epsilon} \right), \quad (4)$$

where  $p_k = \sum_{k \in W_A} |a_k|^2$  with  $|a_k|^2$  is the amplitude component of fundamental mode at site  $k$ , describing the probability of finding a single-quasiparticle state in subsystem  $W_A$ ,  $\epsilon \ll 1$  is inverse of the number of boundary nodes. We plot the measured  $S_S(W_A)$  as a function of  $\theta_A$ , as shown in Fig. 3d. As  $\theta_A$  increases,  $S_S(W_A)$  first grows logarithmically and then asymptotically tends to a constant as  $\theta_A$  approaches  $\pi$ , which is precisely consistent with the theoretical law of equation (3), as demonstrated by the fitted blue line with effective central charge  $c_{eff} = 1.92$  and effective radial cutoff  $a_{eff} = 0.167$  in Fig. 3d. Additionally, we also plot  $S_S(W_A)$  as a function of  $L_{\gamma_D(A)}$  in Fig. 3e, which presents a good linear relation with a slope of  $c_{eff}/6$ , following the zero-



temperature RT formula. Note that the insufficient lattice size in the fabricated hyperbolic circuit does not affect the retrieving of  $c_{eff}$  but introduces a non-zero horizontal intercept in fitted blue line, attributed to a relatively large  $a_{eff}$ . This inconsistency can be efficiently improved by enlarging the lattice radius (see Extended Data Fig. 5).

We then proceed to consider the BBCF in the Poincaré disk which serves as an EAdS<sub>2</sub>/CFT<sub>0+1</sub> setup. According to the AdS/CFT correspondence, the correlation function  $G_S(z_a, z_b)$  between two boundary points  $z_a(\ell, \theta_a)$  and  $z_b(\ell, \theta_b)$  in the bulk weakly-coupled CFT is equal to the correlation function  $G(z_a, z_b)$  between the same two points in the boundary strongly-coupled CFT. Note that  $G(z_1, z_2)$  is known to be determined by the conformal dimension  $\Delta$  via the exponential relation<sup>6,12-15</sup>:

$$G(z_a, z_b) = e^{-\Delta \cdot L_{\gamma_{\mathcal{D}}}(z_a, z_b)} \quad (5)$$

where  $L_{\gamma_{\mathcal{D}}}(z_a, z_b)$  is the geodesic length between two boundary points and  $\Delta$  is associated with the mass  $m_S$  of a bulk scalar field by one-dimensional (1D) KW relation:  $\Delta(\Delta - 1) = m_S^2 \ell^2$ . To test whether  $G_S(z_a, z_b)$  aligns with these CFT conclusions, we experimentally measure  $G_S(z_a, z_b)$  utilizing the scalar field in a type-I hyperbolic circuit. Note that in the long-wavelength limit, the mass-dependent  $G_S(z_a, z_b; m_S)$  in the continuum can be given by the frequency-dependent circuit correlation function  $G_{R_{ab}}(\omega)$  of the type-I hyperbolic circuit (see Methods and Supplementary Information S4.2), and specifically,  $m_S$  is associated with circuit frequency  $\omega$  via the relation  $m_S^2 = -4 / (7\omega^2 LC)$ . In the experiment, as illustrated in the inset of Fig. 3f, we fix the first test point at a boundary node<sub>86</sub> (labelled by  $z_a$ ) and vary the second test point (labelled by  $z_b$ ) along the boundary to change the node-node separation. In stable field consideration, we set input frequency  $f = \omega/2\pi$  above the resonance frequency of fundamental

mode (see Extended Data Fig. 4), which corresponds to the Breitenlohner-Freedman bound<sup>16</sup>. As shown in Fig. 3f, for three different  $m_S^2$ , the measured  $G_S(z_a, z_b)$  (color dots) showcases an exponential dependence on  $L_{\gamma_D(z_a, z_b)}$ , as clearly demonstrated by the well-matched solid lines fitted from  $G_S(z_a, z_b) \propto e^{-\Delta_S \cdot L_{\gamma_D(z_a, z_b)}}$ . Moreover, we also plot the experimentally (pink dots) and numerically (green circles) retrieved scaling dimension  $\Delta_S$  as a function of  $m_S^2$ , as shown in Fig. 3g, the fitted green line demonstrates the best qualitative agreement using KW equation (1) with effective boundary dimension  $d_{b_{eff}} = 1.38$  and effective AdS radius-square  $\ell^2_{eff} = 0.738$ . Inset displays the linear relation between  $\Delta_S(\Delta_S - d_{b_{eff}})$  and  $m_S^2$  with a slope of  $\ell^2_{eff}$ . Note that our fitted  $d_{b_{eff}}$  and  $\ell^2_{eff}$  slightly deviate from the expected value of 1 and 0.84<sup>13,14</sup> because of insufficient boundary discretization in the fabricated hyperbolic circuit. These fitted values will restore to the expected values by enlarging the lattice radius (see Extended Data Fig. 6).

### Measurements of holographic quantities in the type-II hyperbolic circuit

Next, we investigate the case in another disparate AdS<sub>2</sub> background, i.e., the spatial section of a BTZ black hole. We start by considering the BEE in the Poincaré ring which serves as a spatial slice of the AdS<sub>2+1</sub>/CFT<sub>1+1</sub> setup with time fixed. Due to the existence of a black hole and its horizon thermal effects, BEE in this space significantly differs from that of the pure AdS<sub>2</sub> space. As illustrated in the bottom of Fig. 4a, according to the AdS/CFT correspondence, the connection between bulk and boundary entanglement entropy  $S_S(W_A) = S(A)$  still holds. Besides,  $S(A)$  is known to exhibit a more complex logarithmic scaling with the  $A$  size as<sup>3,7</sup>:

$$S(A) \propto \frac{c}{3} \log \left[ \frac{\beta}{\pi a} \sinh \left( \frac{\pi \theta_A}{\beta} \right) \right] \quad (6)$$

where  $\beta = 2\pi/r_h$ ,  $r_h$  is the horizon radius (recovers to equation (3) for zero  $r_h$ ), meanwhile following the 2D finite-temperature RT formula:  $S(A) = \frac{c}{6}L_{\gamma_{\mathcal{R}}(A)}$ , where  $L_{\gamma_{\mathcal{R}}(A)}$  is the length of geodesic  $\gamma_{\mathcal{R}}(A)$  (see Supplementary Information S3.2). To test whether  $S_S(W_A)$  aligns with these CFT conclusions, we adopt the aforementioned strategy (Figs. 3a-c) to experimentally measure  $S_S(W_A)$  by employing the discretized fundamental mode of type-II hyperbolic lattice to reproduce the continuous single-quasiparticle state of scalar field in Poincaré ring, as shown in Figs. 4a-c. Significantly, in this finite-temperature circumstance,  $S_S(W_A)$  can not be computed directly using equation (4) since the entire bulk system is no longer in a pure state. In contrast, the thermal entropy of the horizon also contributes to the total entanglement entropy. Hence, we amend equation (4) into a new form<sup>31</sup>:

$$S_S(W_A) \propto \frac{1}{2} \log \left( \frac{p_k(p_k - 1)}{\epsilon} \right) + \theta_A r_h. \quad (7)$$

when we select the boundary interval as the entire circumference, the first term vanishes and the second term recovers to  $2\pi r_h$ , i.e., the length of the horizon, which is proportional to the famous Bekenstein-Hawking entropy of a black hole. We plot the measured  $S_S(W_A)$  as a function of angle  $\theta_A$ , as shown in Fig. 4d. It is obviously that  $S_S(W_A)$  first increases logarithmically for small  $\theta_A$  and then gradually translates into linear increasing as  $\theta_A$  approaches  $\pi$ , which is precisely consistent with the theoretical law of equation (6), as demonstrated by the fitted blue line with effective central charge  $c_{eff} = 6.3$  and effective radial cutoff  $a_{eff} = 0.143$  in Fig. 4d. Additionally, we also plot  $S_S(W_A)$  as a function of  $L_{\gamma_{\mathcal{R}}(A)}$  in Fig. 4e, which presents a good linear relation with a slope of  $c_{eff}/6$ , following the finite-temperature RT formula. Of particular note is that the insufficient lattice size in the fabricated hyperbolic circuit also does not affect the

retrieving of effective central charge and the non-zero horizontal intercept can also be optimized by enlarging the lattice outer radius (see the first row in Extended Data Fig. 8).

Although the BEE of type-II hyperbolic circuit (Fig. 4d) is significantly distinct from that of the type-I hyperbolic circuit (Fig. 3d), their BBCF showcases the same rule. As shown in Fig. 4f and Fig. 4g, measured  $G_S(z_a, z_b)$  exponentially decay with the geodesic length  $L_{\gamma_{\mathcal{R}}(z_a, z_b)}$  and the retrieved scaling dimension  $\Delta_S$  associates with the scalar field mass  $m_S$  follows KW relation equation (1) with effective boundary dimension  $d_{b_{eff}} = 1.25$  and effective AdS radius-square  $\ell^2_{eff} = 0.652$ . Of particular note is that our fitted  $d_{b_{eff}}$  and  $\ell^2_{eff}$  can also be optimized to expected values of 1 and  $0.84^{13,14}$  by enlarging the outer lattice radius (see Extended Data Fig. 9).

## Discussion

We thus successfully implement the first experimental exploration of the renowned AdS/CFT correspondence in both type-I and type-II hyperbolic lattices, representing disparate spatial geometries of pure  $AdS_{2+1}$  spacetime and  $AdS_{2+1}$  black hole, respectively. Through measuring the BEE and BBCF of scalar fields in hyperbolic lattices, we confirm that these two pivotal quantities indeed reveal behaviors congruent with their holographic counterparts in a CFT, meeting the predictions of the AdS/CFT correspondence. Besides, we have also identified completely different geodesic behaviors in hyperbolic lattices in the presence or absence of an analogue black hole. This work not only expands the fundamental research scope of hyperbolic lattice physics but also provides a new strategy for exploring novel quantum-gravity-inspired phenomena in negatively curved spaces in classical systems. Moreover, this versatile platform offers good opportunities to explore unorthodox and intricate spacetime geometry such as replica wormhole<sup>25,26</sup> and time-

evolving curved space<sup>27</sup>. Straightforward upgrades will enable us to generalize hyperbolic lattices to quantum models by adopting superconducting circuits and quantum qubits to access the real quantum physical effects such as the “ER=EPR” conjecture<sup>28</sup>, and quantum information scrambling<sup>29</sup> in negatively curved spaces.

## References

1. Maldacena, J. The large-N limit of superconformal field theories and supergravity. *Int. J. Theor. Phys.* **38**, 1113 (1999).
2. Witten, E. Anti de sitter space and holography. *Adv. Theor. Math. Phys.* **2**, 253 (1998).
3. Ryu, S. & Takayanagi, T. Holographic derivation of entanglement entropy from the anti-de sitter space/conformal field theory correspondence. *Phys. Rev. Lett.* **96**, 181602 (2006).
4. 't Hooft, G. Dimensional reduction in quantum gravity. Preprint at <https://doi.org/10.48550/arXiv.gr-qc/9310026> (1993).
5. Susskind, L. The World as a hologram. *J. Math. Phys.* **36**, 6377 (1995).
6. Gubser, S. S., Klebanov, I. R. & Polyakov, A. M. Gauge theory correlators from noncritical string theory, *Phys. Lett. B* **428**, 105 (1998).
7. Holzhey, C., Larsen, F. & Wilczek, F. *Nucl. Phys.* **B424**, 443 (1994).
8. Casallerrey-Solana, J. et al. *Gauge/String Duality, Hot QCD and Heavy Ion Collisions* (Cambridge Univ. Press, 2014).
9. Zaanen, J. et al. *Holographic Duality in Condensed Matter Physics* (Cambridge Univ. Press, 2015).
10. Kollár, A. J., Fitzpatrick, M. & Houck, A. A. Hyperbolic lattices in circuit quantum electrodynamics. *Nature* **571**, 45–50 (2019).
11. Lenggenhager, P. M. et al. Simulating hyperbolic space on a circuit board. *Nat. Commun.* **13**, 4373 (2022).
12. Boettcher, I., Bienias, P., Belyansky, R., Kollár, A. J. & Gorshkov, A. V. Quantum simulation of hyperbolic space with circuit quantum electrodynamics: from graphs to geometry. *Phys. Rev. A* **102**, 032208 (2020).
13. Asaduzzaman, M., Catterall, S., Hubisz, J., Nelson, R. & Unmuth-Yockey, J. Holography on tessellations of hyperbolic space. *Phys. Rev. D* **102**, 034511 (2020).
14. Brower, R. C., Coghoun, C. V., Fitzpatrick, A. L., Howarth, D. & Tan, Chung-I. Lattice setup for quantum field theory in AdS<sub>2</sub>. *Phys. Rev. D* **103**, 094507 (2020).
15. Basteiro, P., Boettcher, I., Belyansky, R., Kollár, A. J. & Gorshkov, A. V. Circuit quantum electrodynamics in hyperbolic space: from photon bound states to frustrated spin models. *Phys. Rev. Lett.* **128**, 013601 (2022).

16. Basteiro, P., Dusel, F., Erdmenger, J., Herdt, D., Hinrichsen, H., Meyer, R. & Schrauth, M. Breitenlohner-Freedman Bound on Hyperbolic Tilings. *Phys. Rev. Lett.* **130**, 091604 (2023).
17. Zhang, W., Yuan, H., Sun, N., Sun, H. & Zhang, X. Observation of novel topological states in hyperbolic lattices. *Nat. Commun.* **13**, 2937 (2022).
18. Chen, A. et al. Hyperbolic matter in electrical circuits with tunable complex phases. *Nat. Commun.* **14**, 622 (2022).
19. Zhang, W., Di, F., Zheng, X., Sun, H. & Zhang, X. Hyperbolic band topology with non-trivial second Chern numbers. *Nat. Commun.* **14**, 1083 (2023).
20. Yu, S., Piao, X. & Park, N. Topological hyperbolic lattices. *Phys. Rev. Lett.* **125**, 053901 (2020).
21. Maciejko, J. & Rayan, S. Hyperbolic band theory. *Sci. Adv.* **7**, eabe9170 (2021).
22. Stegmaier, A., Upreti, L. K., Thomale, R. & Boettcher, I. Universality of Hofstadter butterflies on hyperbolic lattices. *Phys. Rev. Lett.* **128**, 166402 (2022).
23. Urwyler, D. M. et al. Hyperbolic Topological Band Insulators. *Phys. Rev. Lett.* **129**, 246402 (2022).
24. Bañados, M., Teitelboim, C. & Zanelli, J. Black hole in three-dimensional spacetime. *Phys. Rev. Lett.* **69**, 1849 (1992).
25. Almheiri, A., Hartman, T., Maldacena, J., Shaghoulian, E. & Tajdini, A. Replica wormholes and the entropy of Hawking radiation. *J. High Energy Phys* **13** (2020).
26. Penington, G., Shenker, S. H., Stanford, D. & Yang, Z. Replica wormholes and the black hole interior. *J. High Energy Phys* **205** (2022).
27. Viermann, C. et al. Quantum field simulator for dynamics in curved spacetime. *Nature* **611**, 260-264 (2022).
28. Jafferis, D. et al. Traversable wormhole dynamics on a quantum processor. *Nature* **612**, 51-55 (2022).
29. Landsman, K. A., Figgatt, C., Schuster, T., Linke, N. M., Yoshida, B., Yao, N. Y. & Monroe, C. Verified quantum information scrambling. *Nature* **567**, 61-65 (2019).
30. Note that hyperboloids plotted in **c** (e.g.  $z^2 - x^2 - y^2 = 1$ ) and **d** (e.g.  $x^2 + y^2 - z^2 = 1$ ) have local negative curvatures but not global constant negative curvatures, they are just schematic diagrams showing two different topologies of curved spaces with constant negative curvatures, which cannot be strictly realized as smooth surfaces in three-dimensional Euclidean space.
31. According to AdS/CFT correspondence, the thermal entropy of entire boundary system is identical to the bulk black hole entropy  $S_{BH} \propto 2\pi r_h$ . The thermal entropy in the boundary theory is an extensive quantity and will be proportional to the size of the subsystem. Therefore, its dual bulk thermal entropy  $S_s(W_A)_T \propto \theta_A r_h$ .

## Main figure legends

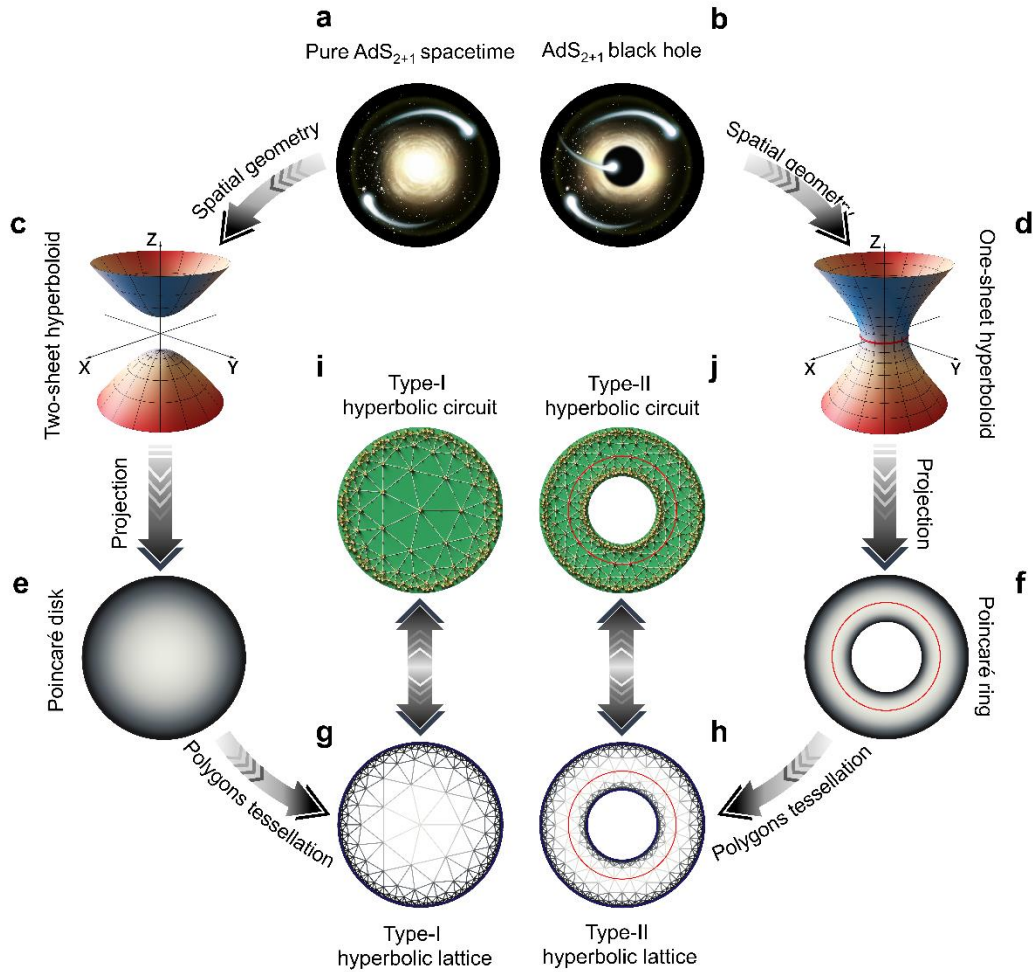


**Fig. 1 | From  $AdS_{2+1}$  spacetimes to hyperbolic lattices.** **a, b**, Schematic illustrations of pure  $AdS_{2+1}$  spacetime (**a**) and  $AdS_{2+1}$  black hole (**b**). **c, d**, Two-sheet hyperboloid (**c**) and one-sheet hyperboloid (**d**), which are spatial geometries of **a** and **b**, respectively. The red circle in **d** indicates the location with the minimum radius on the surface. **e, f**, Poincaré disk (**e**) and ring (**f**) models, which are projective planar counterparts of **c** and **d**, respectively. **g, h**, Type-I (**g**) and type-II (**f**) hyperbolic lattices, which are lattice regularizations of **e** and **f**, respectively. The red circle in **f** and **h** is the exact counterpart in **d** which indicates the horizon. **i, j**, Type-I (**i**) and Type-II (**j**) hyperbolic circuits which are circuit equivalents of **g** and **h**, respectively.

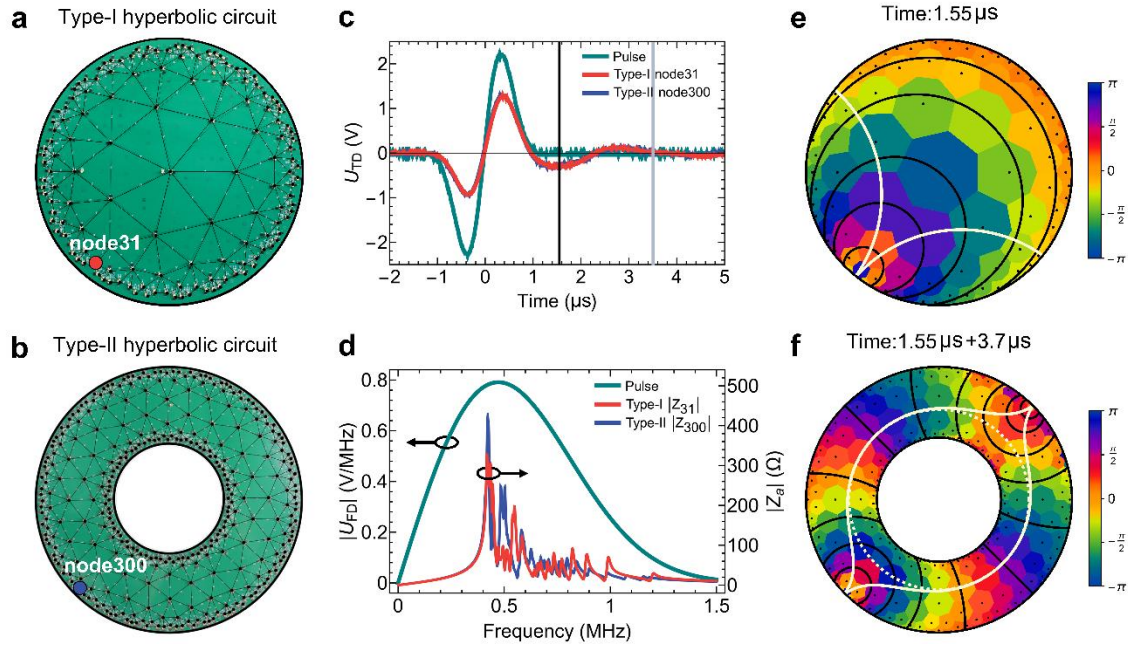


**Fig. 2 | Time-dynamic measurements of geodesics in two hyperbolic circuits.** **a, b**, Photographs of the fabricated type-I (**a**) and type-II (**b**) hyperbolic circuits. Inset red and blue dots represent signal input nodes. **c**, Measured voltage excitation pulse (green line) and voltage response pulses (red and blue lines) at the input nodes. The vertical black line indicates the time of measuring the instantaneous phase profiles in **e**. The vertical black and grey lines indicate the time of measuring the instantaneous phase profiles in **f**. **d**, Measured frequency spectrum of the excitation pulse (green line) and the impedance to ground at the input nodes (red and blue lines). **e, f**, Measured instantaneous phase profiles (background color map) of the pulse propagating in type-I (**e**) and type-II (**f**) hyperbolic circuits at time  $1.55\mu\text{s}$  and  $1.55\mu\text{s} + 3.7\mu\text{s}$ , respectively, small black dots represent the nodes, black arcs represent the phase fronts and white solid curves indicate the geodesics. The white dashed circle in **f** represents the horizon.



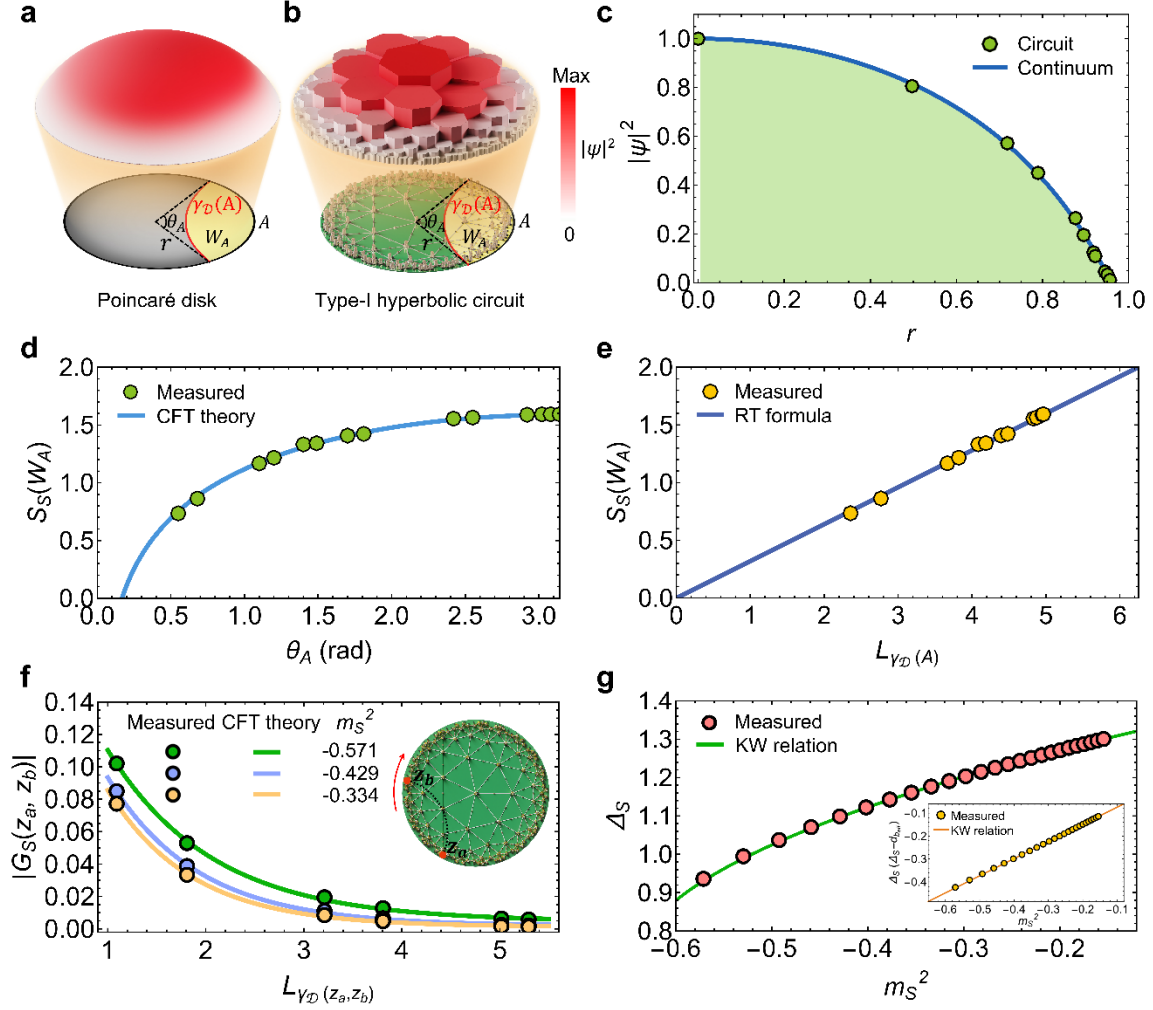


**Fig. 3 | Experimental measurements of BEE and BBCF in type-I hyperbolic circuit.** **a**, Theoretical continuous fundamental mode of a scalar field in Poincaré disk. **b**, Measured discretized fundamental mode of a scalar field in type-I hyperbolic circuit. The insets in **a** and **b** illustrate the boundary subsystems  $A$  (black interval) and corresponding entanglement wedge  $W_A$  (yellow region), the red arc represents the anchored geodesic  $\gamma_D(A)$ . **c**, Comparison of the radial profiles of modes in **a** and **b**. **d**, Measured BEE  $S_S(W_A)$  (green octagons) versus angle  $\theta_A$ , the blue line is a theoretical fitting of CFT equation (3). **e**, Measured BEE  $S_S(W_A)$  (orange octagons) versus geodesic length  $L_{\gamma_D(A)}$ , the dark blue line is a linear fitting. **f**, Measured BBCF  $G_S(z_a, z_b)$  (color dots) versus geodesic length  $L_{\gamma_D(z_a, z_b)}$  for three different mass-squared  $m_S^2$ , color solid lines are exponential law fittings. Inset illustrates the measurement process of  $G_S(z_a, z_b)$ . **g**, Measured conformal dimension  $\Delta_S$  (pink dots) versus mass-squared  $m_S^2$ , the green solid line is a theoretical fitting of CFT equation (1). Inset displays the linear relation between  $\Delta_S(\Delta_S - d_{b_{eff}})$  and  $m_S^2$ .

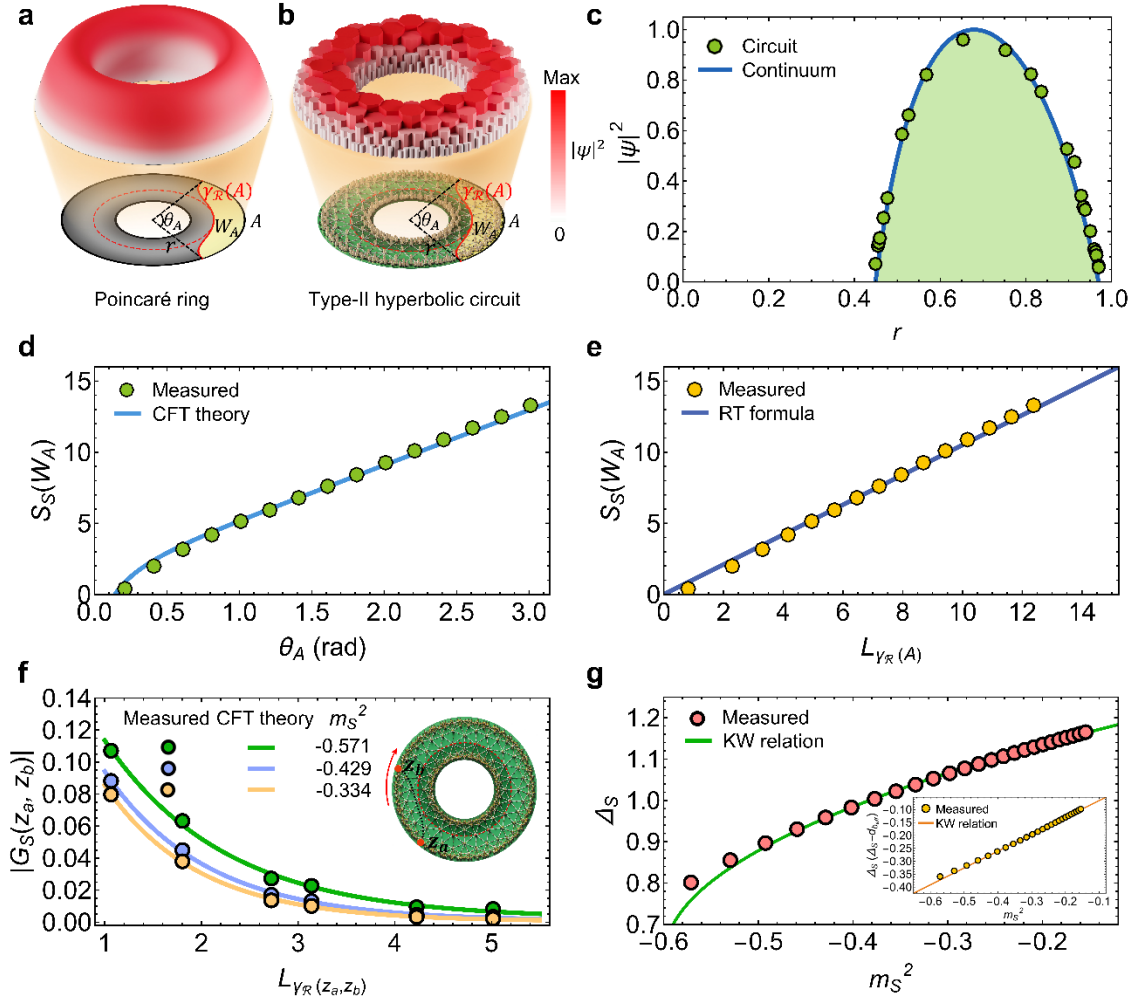


**Fig. 4 | Experimental measurement of BEE and BCF in type-II hyperbolic circuit.** **a**, Theoretical continuous fundamental mode of a scalar field in Poincaré ring. **b**, Measured discretized fundamental mode of a scalar field in type-II hyperbolic circuit. The insets in **a** and **b** illustrate the boundary subsystems  $A$  (black interval) and corresponding entanglement wedge  $W_A$  (yellow region), the red arc represents the anchored geodesic  $\gamma_{\mathcal{R}}(A)$ . **c**, Comparison of the radial profiles of modes in **a** and **b**. **d**, Measured BEE  $S_S(W_A)$  (green octagons) versus angle  $\theta_A$ , the blue line is a theoretical fitting of CFT equation (6). **e**, Measured BEE  $S_S(W_A)$  (orange octagons) versus geodesic length  $L_{\gamma_{\mathcal{R}}(A)}$ , the dark blue line is a linear fitting. **f**, Measured BCF  $G_S(z_a, z_b)$  (color dots) versus geodesic length  $L_{\gamma_{\mathcal{R}}(z_a, z_b)}$  for three different mass-squared  $m_S^2$ , color solid lines are exponential law fittings. Inset illustrates the measurement process of  $G_S(z_a, z_b)$ . **g**, Measured conformal dimension  $\Delta_S$  (pink dots) versus mass-squared  $m_S^2$ , the green solid line is a theoretical fitting of CFT equation (1). Inset displays the linear relation between  $\Delta_S(\Delta_S - d_{b_{eff}})$  and  $m_S^2$ .

## **Acknowledgments**

Z.G. acknowledges funding from the National Natural Science Foundation of China (grant no. 6231101016, 62375118, and 12104211), Shenzhen Science and Technology Innovation Commission (grant no. 20220815111105001), and SUSTech (grant no. Y01236148 and no. Y01236248). Y.H.Y acknowledges funding from the Key Research and Development Program of the Ministry of Science and Technology (grant no. 2022YFA1404704 (H.C.), 2022YFA1404902 (Y.Y.) and 2022YFA1405201 (Y.Y.)), the National Natural Science Foundation of China (grant no.11961141010 (H.C.), no. 62175215 (Y.Y.) and no. 61975176 (H.C.)), the Fundamental Research Funds for the Central Universities (2021FZZX001-19) (Y.Y.), and the Excellent Young Scientists Fund Program (Overseas) of China (Y.Y.). R.-Q.Y acknowledges funding from National Natural Science Foundation of China (grant no. 12005155). Y.T.Y acknowledges funding from Natural Science Foundation of Jiangsu Province (grant no. BK20200630) and National Natural Science Foundation of China (grant no. 12004425). R.-G.C. acknowledges funding from National Natural Science Foundation of China (grant. no. 11821505).

## **Author contributions**

Z.G. and Y.H.Y. initiated the project. J.C. F.C. and R.-Q.Y. performed the theoretical calculation. Z.G., J.C., and Y.T.Y designed the experiments. J.C. and Z.G. fabricated the samples. J.C. and Z. C. carried out the measurements. J.C., L.Y., Y.M., B.Y., X.X., X.Z., G.-G.L., P.P.S., H.C., R.-G.C., R.-Q.Y., Y.H.Y., and Z.G. analyzed the results. J.C. and Z.G. wrote the manuscript with input from all authors. Z.G., J.C., Y.H.Y., R.-Q.Y. and R.-G.C. revised the manuscript. Z.G., Y.H.Y., and R.-Q.Y. supervised the project.

## **Competing interests**

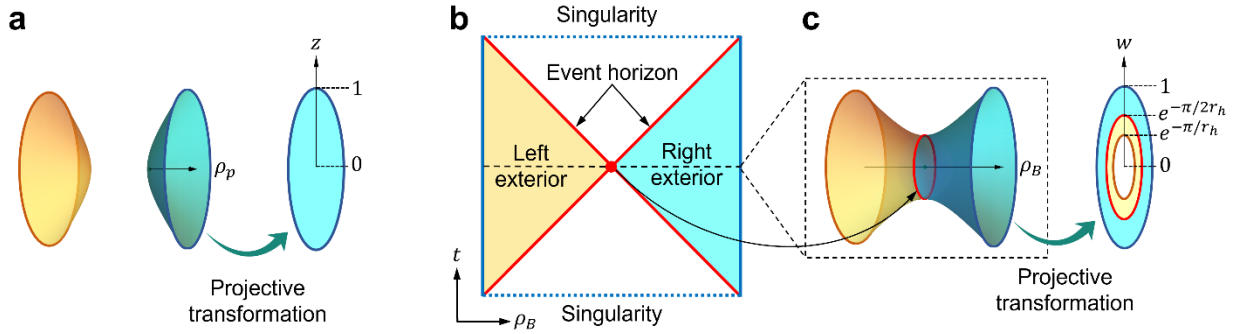
The authors declare no competing interests.

**Correspondence and requests for materials** should be addressed to Zhen Gao, Yihao Yang and Run-Qiu Yang.

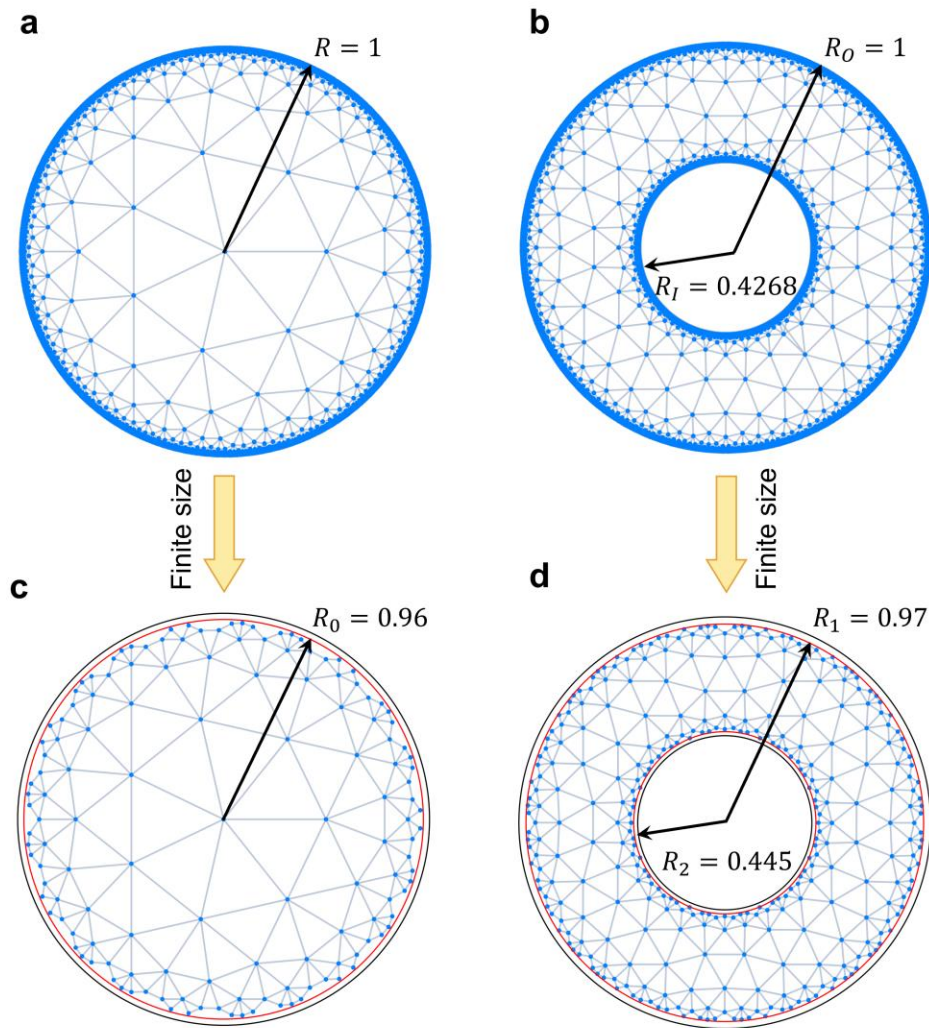
## **Data availability**

All data that support the plots within this paper and other finding of this study are available from the corresponding authors upon reasonable request.

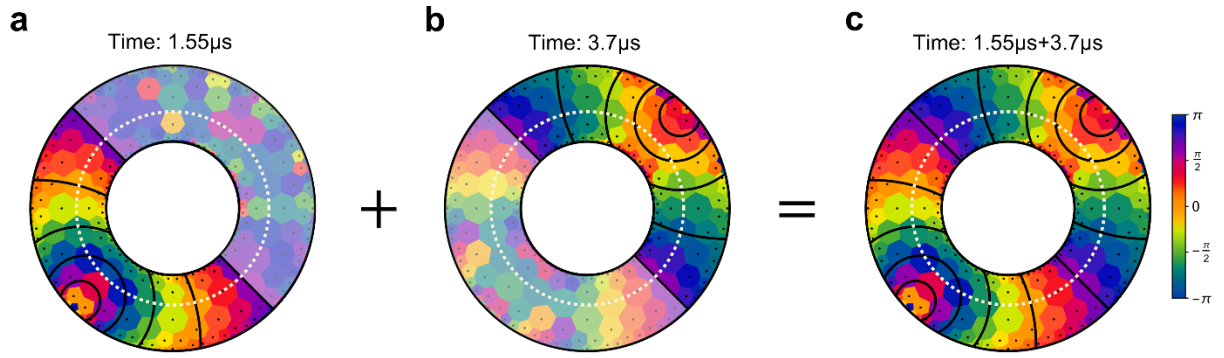
## Extended data figure legends



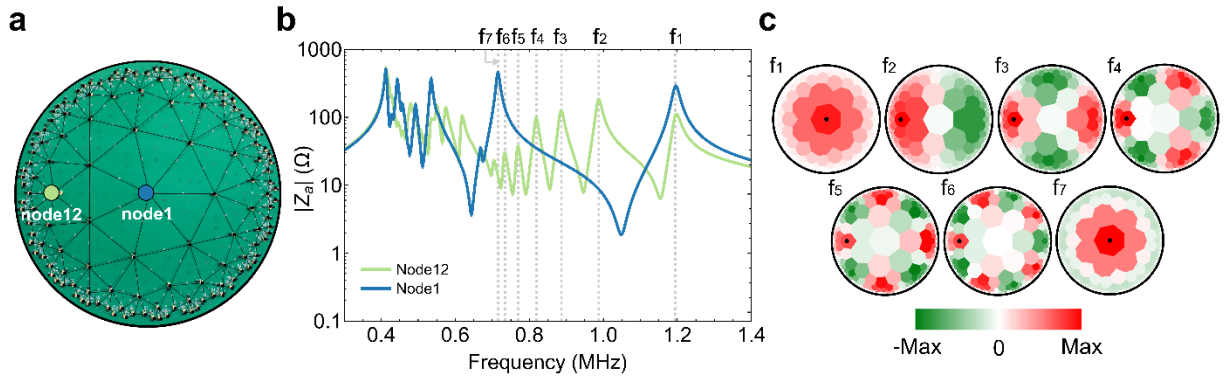
**Extended Data Fig. 1 | Spatial geometries and topologies of  $\text{AdS}_{2+1}$  spacetimes.** **a**, The geometry of a spatial slice in pure  $\text{AdS}_{2+1}$  spacetime manifests as one branch of a two-sheet hyperboloid with constant negative curvature, or as a planar Poincaré disk. **b**, Penrose diagram of a BTZ black hole. The red solid lines represent the entire horizon and the horizontal dashed line indicates a spatial slice at  $t = 0$ . **c**, The geometry of the spatial slice in **b** manifests as a one-sheet hyperboloid with constant negative curvature, or as a planar Poincaré ring, the red circle in each panel represents the partial horizon, corresponding to the origin point (red dot) in **b**.



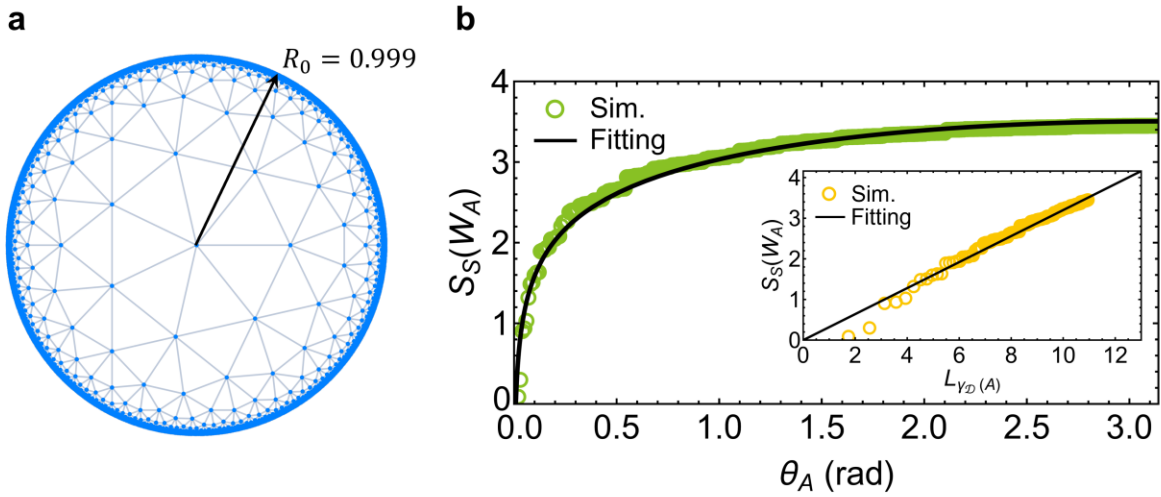
**Extended Data Fig. 2 | Ideal and practical type-I and type-II hyperbolic lattices with  $\{3,7\}$  regular tessellation.** **a**, Ideal type-I hyperbolic lattice with maximal radius  $R = 1$ . **b**, Ideal type-II hyperbolic lattice (we here set horizon radius  $r_h = 3.69$ ) with maximal radius  $R_O = 1$  and minimal radius  $R_I = e^{-\pi/r_h} \approx 0.4268$ . **c**, Practical type-I hyperbolic lattice we adopted in the main text with maximal radius  $R_0 = 0.97$  and 141 sites in total. **d**, Practical type-II hyperbolic lattice we adopt in the main text with maximal radius  $R_1 = 0.97$ , minimal radius  $R_2 = 0.445$  and 336 sites in total.



**Extended Data Fig. 3 | Reconstitution for the measured instantaneous phase profile of type-II hyperbolic circuit in Fig. 2f. a, b**, Measured instantaneous phase profiles of a pulse propagating on the type-II hyperbolic circuit at time  $1.55\mu\text{s}$  (**a**) and  $3.7\mu\text{s}$  (**b**). The semi-transparent white regions in **a** and **b** indicate that the pulse has not arrived (measured instantaneous phase profile is disordered) or has left (measured instantaneous phase profile reverts to be disordered). **c**, Combination of effective instantaneous phases (color polygons) and phase fronts (black arcs) in **a** and **b**, both values of phases at the joint are approximately equivalent.

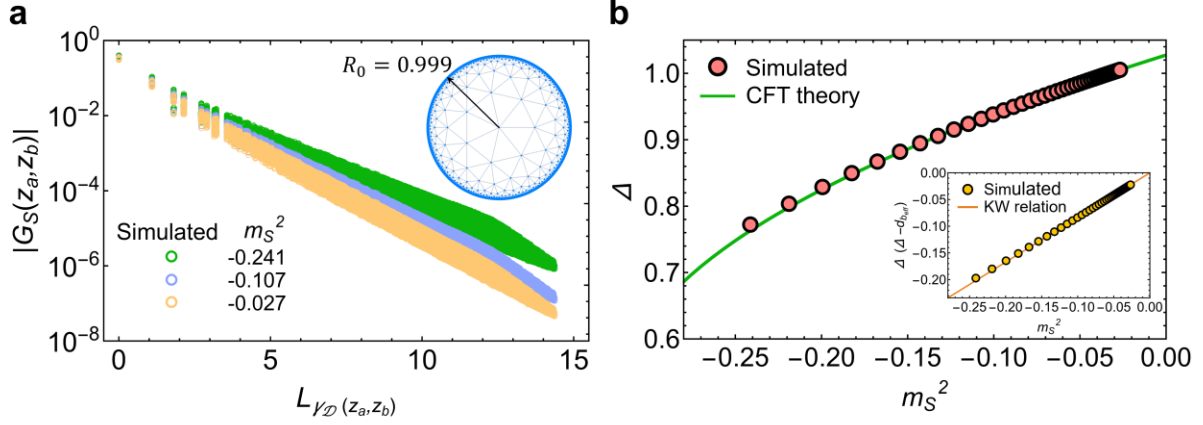


**Extended Data Fig. 4 | Measurement of intrinsic resonance in type-I hyperbolic circuit. a,** Illustration of test nodes in the type-I hyperbolic circuit. **b,** Measured impedance spectrum to the ground for different nodes in **a**, the vertical grey dashed lines indicate the highest seven resonance peaks. **c,** Measured voltage profiles of first seven eigenmodes corresponding to the resonance frequencies in **b**.



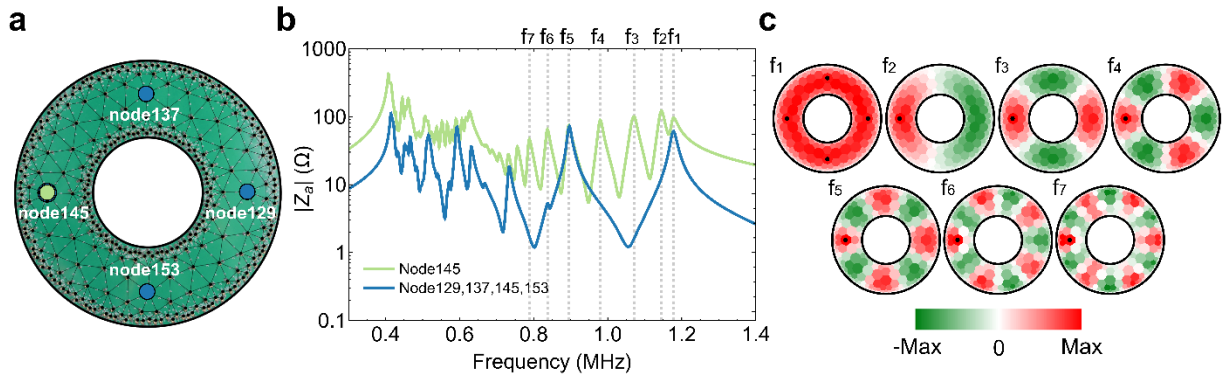
**Extended Data Fig. 5 | Numerical simulation of BEE in quasi-ideal type-I hyperbolic circuit.**  
**a**, Quasi-ideal type-I hyperbolic circuit with maximal radius  $R_0 = 0.999$  and 5962 sites in total.  
**b**, Simulated BBE  $S_S(W_A)$  (green circles) versus angle  $\theta_A$ , the black line is a theoretical fitting of equation (3) with effective central charge  $c_{eff} = 1.92$  and effective radial cutoff  $a_{eff} = 0.00838$ . Inset displays the linear relation between  $S_S(W_A)$  and the geodesic length  $L_{\gamma_D(A)}$ .



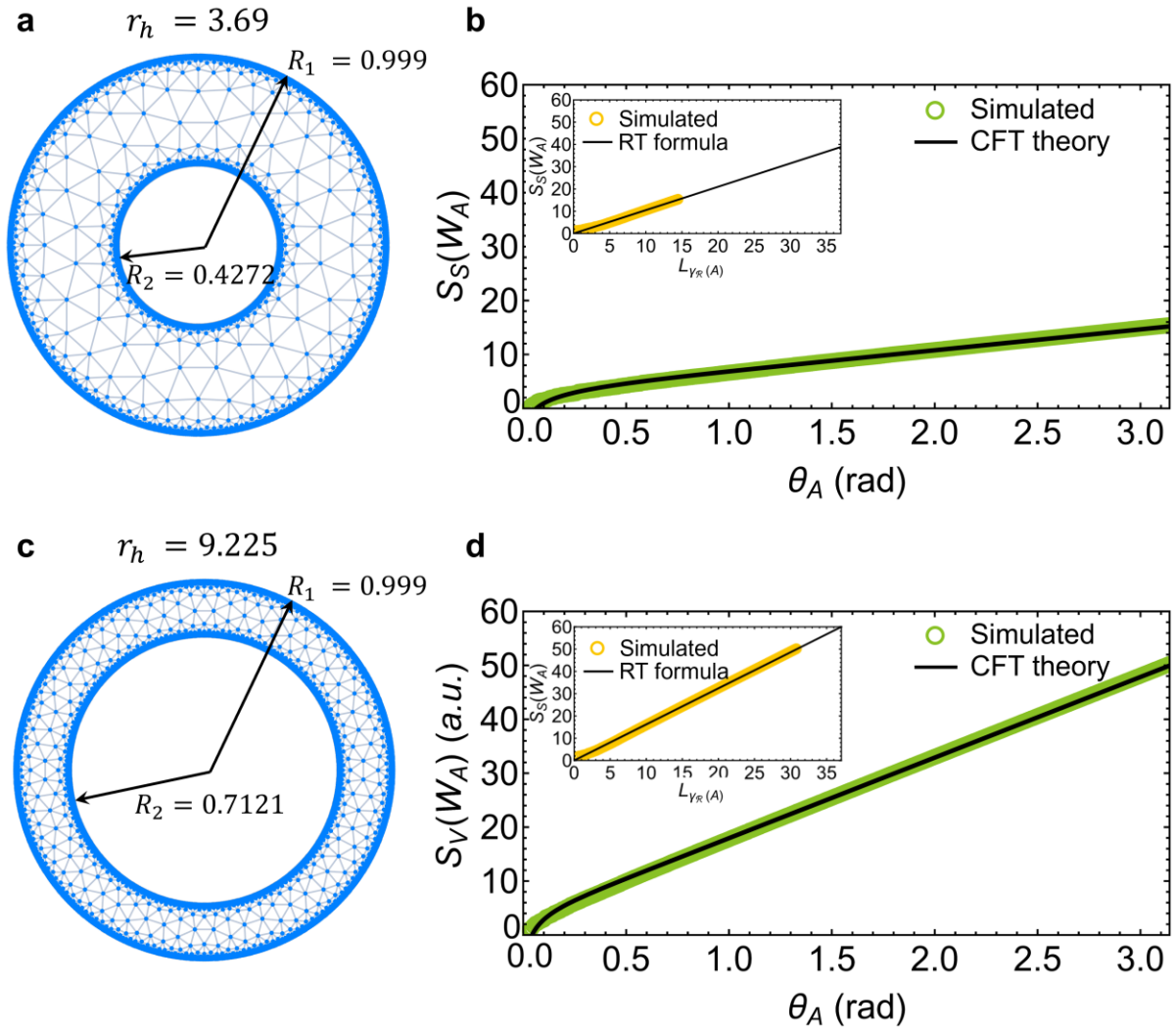


**Extended Data Fig. 6 | Numerical simulation of BBCF in quasi-ideal type-I hyperbolic circuit.**

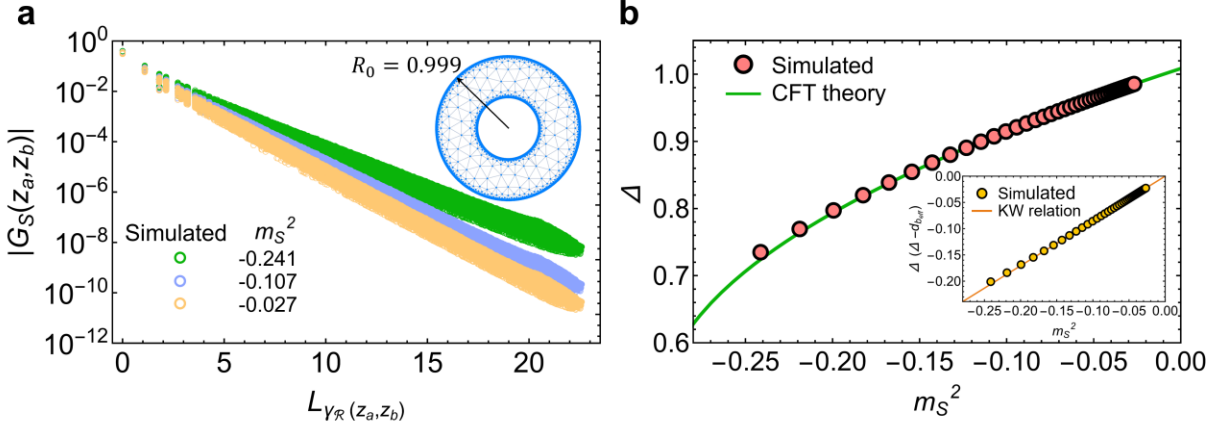
**a**, Logarithmic plots of simulated BBCF  $G_S(z_a, z_b)$  as an exponential function of hyperbolic distance  $L_{\gamma_D}(z_a, z_b)$  for three different mass-squared  $m_S^2$ . Inset shows the same quasi-ideal type-I hyperbolic circuit in Extended Data Fig. 5a. **b**, Simulated conformal dimension  $\Delta$  (pink dots) verse mass-squared  $m_{eff}^2$ , the green line is a theoretical fitting of equation (1) with effective boundary dimension  $d_{b_{eff}} = 1.028$  and effective AdS radius-squared  $\ell_{eff}^2 = 0.836$ . Inset displays the linear relation between  $\Delta(\Delta - d_{b_{eff}})$  and  $m_S^2$ .



**Extended Data Fig. 7 | Measurement of intrinsic resonance in type-II hyperbolic circuit. a,** Illustration of test nodes in the type-II hyperbolic circuit. **b,** Measured impedance spectrum to the ground for different nodes in **a**, the vertical grey dashed lines indicate the highest seven resonance peaks. **c,** Measured voltage profiles of first seven eigenmodes corresponding to the resonance frequencies in **b**.



**Extended Data Fig. 8 | Numerical simulation of BEE in quasi-ideal type-I hyperbolic circuits with different horizon radii.** **a**, Quasi-ideal type-II hyperbolic circuit with horizon radius  $r_h = 3.69$ , maximal radius  $R_1 = 0.999$ , minimal radius  $R_2 = 0.4272$  and 11952 sites in total. **b**, Simulated BBE  $S_S(W_A)$  (green circles) verse angle  $\theta_A$ , the black line is a theoretical fitting of equation (6) with effective central charge  $c_{eff} = 6.3$  and effective outer radial cutoff  $a_{eff} = 0.0641$ . **c**, Quasi-ideal type-II hyperbolic lattice with larger horizon radius  $r_h = 9.225$ , maximal radius  $R_1 = 0.999$ , minimal radius  $R_2 = 0.7121$  and 12040 sites in total. **d**, Simulated BEE  $S_S(W_A)$  (green circles) verse angle  $\theta_A$ , the black line is a theoretical fitting of equation (6) with effective central charge  $c_{eff} = 9.72$  and effective outer radial cutoff  $a_{eff} = 0.0429$ . Inset in **b** or **d** displays linear relation between the  $S_S(W_A)$  and the geodesic length  $L_{\gamma_R(A)}$ .



**Extended Data Fig. 9 | Numerical simulation of BBCF in quasi-ideal type-II hyperbolic circuit.** **a**, Logarithmic plots of simulated BBCF  $G_S(z_a, z_b)$  as an exponential function of hyperbolic distance  $L_{\gamma_{\mathcal{R}}}(z_a, z_b)$  for three different mass-squared  $m_S^2$ . Inset shows the same quasi-ideal type-II hyperbolic circuit in Extended Data Fig. 8a. **b**, Simulated conformal dimension  $\Delta$  (pink dots) verse mass-squared  $m_{eff}^2$ , the green line is a theoretical fitting of equation (1) with effective boundary dimension  $d_{b_{eff}} = 1.008$  and effective AdS radius-squared  $\ell_{eff}^2 = 0.853$ . Inset displays the linear relation between  $\Delta(\Delta - d_{b_{eff}})$  and  $m_S^2$

<b>Massive scalar field</b>	<b>Hyperbolic circuit</b>
Field $\phi(z)$	Voltage $V_a$
Action $\Gamma_s(z)$	Reduced circuit power $P_R$
Laplace-Beltrami operator $\Delta_s$	Reduced grounded circuit Laplacian $J_{Rab}$
Correlation function $G_s(z_a, z_b)$	Circuit correlation function $G_{Rab}$
Mass-squared $m_s^2$	Circuit resonance frequency $-\frac{4}{q\omega^2 LC}$

**Extended Data Table 1 | Summary of equivalents of massive scalar field quantities in the hyperbolic circuit.**

**End**